Geosci. Model Dev. Discuss., 7, 7267–7316, 2014
www.geosci-model-dev-discuss.net/7/7267/2014/
doi:10.5194/gmdd-7-7267-2014

Geoscientific Model Development Discussions
Open Access

EDDA: integrated simulation of debris flow erosion, deposition and property changes

H. X. Chen and L. M. Zhang

Department of Civil and Environmental Engineering, The Hong Kong University of Science and Technology, Clear Water Bay, Hong Kong

Received: 20 August 2014 – Accepted: 10 October 2014 – Published: 4 November 2014

Correspondence to: L. M. Zhang (cezhangl@ust.hk)

Published by Copernicus Publications on behalf of the European Geosciences Union.

Abstract

Debris flow material properties change during the initiation, transportation and deposition processes, which influences the runout characteristics of the debris flow. A quasi-three-dimensional depth-integrated numerical model, EDDA, is presented in this paper to simulate debris flow erosion, deposition and induced material property changes. The model considers changes in debris flow density, yield stress and dynamic viscosity during the flow process. The yield stress of debris flow mixture is determined at limit equilibrium using the Mohr–Coulomb equation, which is applicable to clear water flow, hyper-concentrated flow and fully developed debris flow. To assure numerical stability and computational efficiency at the same time, a variable time stepping algorithm is developed to solve the governing differential equations. Four numerical tests are conducted to validate the model. The first two tests involve a one-dimensional dam-break water flow and a one-dimensional debris flow with constant properties. The last two tests involve erosion and deposition, and the movement of multi-directional debris flows. The changes in debris flow mass and properties due to either erosion or deposition are shown to affect the runout characteristics significantly. The model is also applied to simulate a large-scale debris flow in Xiaojiagou Ravine to test the performance of the model in catchment-scale simulations. The results suggest that the model estimates well the volume, inundated area, and runout distance of the debris flow. The model is intended for use as a module in a real-time debris flow warning system.

1 Introduction

Debris flow is a flow of a sediment-water mixture driven by gravity. The mechanical triggers of debris flows can be classified into three types; namely, erosion by surface runoff, transformation from landslides, and collapse of debris dams (Takahashi, 2007). The volume of debris flow can increase due to basal erosion or surficial material entrainment during the marching process; the final volume can be several or dozens times

GMDD
7, 7267–7316, 2014

of the initial volume (e.g. Hungr et al., 2005; Chen et al., 2006, 2012, 2014; Berger et al., 2010). When the debris flow moves to a flatter area, the coarse materials can deposit gradually. During the entire movement process, not only the debris flow volume, flow velocity and flow depth change significantly, the properties of the debris flow mixture also change substantially, which may highly influence the runout characteristics.

The mechanisms of changes in debris flow mass are important and have attracted the attention of many researchers (e.g. Cannon and Savage, 1988; Takahashi et al., 1992; Hungr, 1995; Egashira et al., 2001; Iverson, 2012). Cannon and Savage (1988) and Hungr (1995) proposed one-dimensional lumped-mass models based on momentum conservation to describe the entrainment or loss of material during the movement of a debris flow. Takahashi et al. (1992) proposed a model to describe erosion and deposition based on volumetric sediment concentration and flow velocity. Researchers have also described the erosion process from a stress point of view (e.g. Egashira et al., 2001; Iverson, 2012). Erosion occurs when the basal shear stress exceeds the critical erosive shear stress of the bedding material.

During the entire process of a debris flow, the debris flow properties can change significantly. The volumetric sediment concentration (i.e. ratio of the solid volume to the total volume of the debris flow mixture) can increase substantially due to entrainment of solid materials (e.g. Takahashi et al., 1992; Egashira et al., 2001) and can decrease due to deposition (e.g. Takahashi et al., 1992) or dilution (e.g. Pierson and Scott, 1985). Accordingly, the rheological characteristics of debris flows (e.g. yield stress and dynamic viscosity) will change with the volumetric sediment concentration, which has been observed in a large number of experiments (e.g. O'Brien and Julien, 1988; Rickenmann, 1991; Major and Pierson, 1992; Sosio and Crosta, 2009; Bisantino et al., 2010). Various rheological models have been adopted to describe debris flows, such as the laminar flow model (e.g. Takahashi, 2007), the Bingham fluid model (e.g. Fraccarollo and Papa, 2000), the Voellmy model (e.g. Medina et al., 2008), and the quadratic rheological model (Julien and Lan, 1991).

GMDD
7, 7267–7316, 2014

Based on understanding of erosion, deposition and rheology of debris flow materials, great efforts have been made to simulate the movement of debris flows (e.g. Cannon and Savage, 1988; Takahashi et al., 1992; Li et al., 2012; Pastor et al., 2009; Hungr, 1995; Denlinger and Iverson, 2001; Ghilardi et al., 2001; Chen et al., 2006, 2013; van Asch et al., 2014). The numerical methods include the finite difference method (e.g. Takahashi et al., 1992), the finite volume method (e.g. Medina et al., 2008), the finite element method (e.g. Crosta et al., 2003), the distinct element method (e.g. Li et al., 2012), the smoothed particle hydrodynamics method (e.g. Pastor et al., 2009) and others. Several computer programs have been written for debris flow analysis, such as DAMBRK (Boss Corporation, 1989), FLO-2D (O'Brien et al., 1993), DAN (Hungr, 1995), TOCHNOG (Crosta et al., 2003), 3dDMM (Kwan and Sun, 2006), FLATModel (Medina et al., 2008), DAN3D (Hungr and McDougall, 2009), MassMov2D (Beguería et al., 2009), PASTOR (Pastor et al., 2009), and RAMMS (Bartelt et al., 2013). The changes in flow depth, flow velocity and debris mass have been accounted for in these programs. Limited attempt has also been made to consider the evolution of volumetric sediment concentration (Takahashi et al., 1992; Denlinger and Iverson, 2001; Ghilardi et al., 2001). Some key problems, however, still remain. How can one describe the various phases of a debris flow (e.g. clear water flow, hyper-concentrated flow, and fully developed debris flow) using a general rheological model? How do the properties of debris flows (e.g. volumetric sediment concentration, yield stress, viscosity) change in the erosion and deposition processes? How do these changes affect the runout characteristics of the debris flow? These problems are very important for the risk assessment of debris flows.

The objective of this paper is to develop a numerical model to consider the erosion and deposition processes and debris flow property changes during these processes. The paper is organized as follows. The methodology is introduced in Sect. 2, including the problem description, governing equations, constitutive models, initiation of erosion and deposition, numerical solution algorithm, time stepping and numerical stability. The model is tested and verified in Sect. 3 using analytical solutions and experimental tests.

GMDD
7, 7267–7316, 2014

A large-scale debris flow event in the Wenchuan earthquake zone is simulated as a field application in Sect. 4. The limitations of the model are indicated in Sect. 5.

2 Methodology

2.1 Problem description

The volume of a debris flow can increase due to erosion or entrainment and decrease due to deposition. Due to changes in sediment concentration, a debris flow triggered by surface runoff may experience several flow regimes. The debris flow can evolve from a clear water flow to a hyper-concentrated flow, a fully developed debris flow, and finally a deposit on the debris fan. The erosion and deposition processes and property changes in debris flow are illustrated in Fig. 1. The debris flow entrains and incorporates materials from the channel bed if the volumetric sediment concentration, C_v, is smaller than an equilibrium value, $C_{v\infty}$, for the channel gradient, and some material separates from the debris flow mixture and deposits on the channel bed when the volumetric sediment concentration is larger than an equilibrium value for the channel gradient and the flow velocity is not large enough to take all the material. Due to erosion and deposition, debris flow properties change significantly. The changes in the volumetric sediment concentration, yield stress and viscosity are shown in Figs. 2 and 3. When it is a clear water flow, only a small amount of solid particles moves with the flow. The yield stress is negligible, and the dynamic viscosity is close to that of water. When solid materials are entrained into the flow due to erosion, the flow may evolve into a hyper-concentrated flow. The flow develops a significant yield stress, and the dynamic viscosity increases to a certain level. A debris flow can fully develop after sufficient solid materials are entrained into the flow. The yield stress and dynamic viscosity increase to relatively high levels. The debris flow will decelerate when moving to a flatter area, and deposition occurs along the flow path. The volumetric sediment concentration decreases in the deposition process.

GMDD
7, 7267–7316, 2014

2.2 Governing differential equations

In this study, an integrated numerical model is developed to simulate debris flow erosion, deposition, and the induced property changes. The model is named as EDDA, which stands for erosion (E), deposition (D) debris flow analysis (DA). The reference frame is defined in Fig. 1. Depth-integrated mass conservation equations (Eqs. 1 and 2) and a momentum conservation equation (Eq. 3) are adopted to describe the movement of a debris flow (Takahashi et al., 1992; Egashira et al., 2001):

$$\frac{\partial h}{\partial t} + \frac{\partial (hv)}{\partial x} = i[C_{v*} + (1 - C_{v*})s_b], \tag{1}$$

$$\frac{\partial (C_v h)}{\partial t} + \frac{\partial (C_v hv)}{\partial x} = iC_{v*}, \tag{2}$$

$$\frac{\partial v}{\partial t} + v\frac{\partial v}{\partial x} = g\left[-\mathrm{sgn}(v)S_f - \frac{\partial (z_b + h)}{\partial x}\right] - \frac{vi[C_{v*} + (1 - C_{v*})s_b]}{h}, \tag{3}$$

where h is the flow depth; t is time; v is the depth-averaged flow velocity in one of four compass directions (i.e. north, east, south and west in Fig. 4) and four diagonal directions (i.e. northeast, southeast, southwest and northwest in Fig. 4); i is the erosion rate (> 0) or deposition rate (< 0); C_{v*} is the volume fraction of solids in the erodible bed; s_b is the degree of saturation of the erodible bed; C_v is the volumetric sediment concentration of the debris flow mixture; g is the gravitational acceleration; S_f is the flow resistance slope; and z_b is the bed elevation; the sgn (i.e. signum) function is used to make sure the direction of the flow resistance is opposite to that of the flow direction. The bed elevation changes in the erosion and deposition processes, and can be expressed as

$$\frac{\partial z_b}{\partial t} = -i. \tag{4}$$

GMDD
7, 7267–7316, 2014

2.3 Constitutive models

Various forms of rheological models can be implmented in the momentum conservation equation, which allows the simulution of various types of flows. Several most widely used rheological models are introduced below to compute S_f; namely, the laminar flow model, the turbulent flow model, the Bingham fluid model, the Voellmy model, and the quadratic rheological model.

The laminar flow model is useful to describe the movement of a fully liquefied flow, which is governed by viscous behaviour. The flow resistance slope is expressed as

$$S_f = \frac{K\mu V}{8\rho g h^2}, \tag{5}$$

where K is a resistance parameter for laminar flow; μ is the dynamic viscosity; V is the absolute value of flow velocity; ρ is the debris flow density; g is the gravitional acceleration.

Turbulent flows with low volumetric sediment concentration are often analyzed using the Manning equation:

$$S_f = \frac{n^2 V^2}{h^{4/3}}, \tag{6}$$

where n is the Manning coefficient.

The Bingham fluid model conisders both plastic and viscous behaviours. A Bingham fluid does not move if the shear stress is smaller than a threshold yield strength, but behaves as a viscous material when the shear stress exceeds the threshold. The model is expressed as

$$S_f = \frac{\tau_0}{\rho g h}, \tag{7}$$

GMDD
7, 7267–7316, 2014
EDDA

H. X. Chen and
L. M. Zhang

where

$$2\tau_0^3 - 3\left(\tau_y + 2\frac{\mu V}{h}\right)\tau_0^2 + \tau_y^3 = 0, \tag{8}$$

where τ_0 is the basal shear stress; τ_y is the yield stress of debris flow.

The Voellmy model (Voellmy, 1955) combines the effects of frictional and turluent behaviours:

$$S_f = \cos\theta \tan\phi + \frac{V^2}{\xi h}, \tag{9}$$

where θ is the bed slope; ϕ is the friction angle of the solid particles contacting the bed; ξ is a turbulence parameter.

The quadratic rheological model proposed by Julien and Lan (1991) considers the effects of frictional behaviour, viscous behaviour, and turbulent behaviour plus the resistance arising from solid-particle contacts, which are represented by three terms as follows:

$$S_f = \frac{\tau_y}{\rho g h} + \frac{K\mu V}{8\rho g h^2} + \frac{n_{td}^2 V^2}{h^{4/3}}, \tag{10}$$

where n_{td} is the equivalent Manning coefficient, which accounts for both the turbulent behaviour and the resistance arising from solid-particle contacts and is expressed as (FLO-2D Software Inc., 2009)

$$n_{td} = 0.0538 n e^{6.0896 C_v}. \tag{11}$$

Since the quadratic rheological model accounts for the most comprehensive flow behaviour, it is adopted into the governing differential equations in this paper.

GMDD
7, 7267–7316, 2014
EDDA

H. X. Chen and
L. M. Zhang

O'Brien and Julien (1988) proposed the following empirical relationships to estimate the dynamic viscosity, μ, and the yield stress, τ_y, based on laboratory tests:

$$\mu = \alpha_1 e^{\beta_1 C_v}, \quad (12)$$

$$\tau_y = \alpha_2 e^{\beta_2 C_v}, \quad (13)$$

where α_1, α_2, β_1 and β_2 are empirical coefficients. The equations describe well the changes of μ and τ_y with C_v when the C_v value is sufficiently large. But for very small C_v values (e.g. 0 for water), Eqs. (12) and (13) give α_1 and α_2, respectively, while in reality μ and τ_y are 0.001 Pa s at 20 °C and 0, respectively when C_v is 0. Moreover, the yield stress increases with flow depth, which cannot be captured by Eq. (13). In this study, a new equation is derived to estimate τ_y. Assuming a hydrostatic pressure distribution within the debris flow, the effective normal stress on the inclined channel bed is

$$\sigma = C_v(\rho_s - \rho_w)gh\cos^2\theta, \quad (14)$$

where ρ_s is the density of solid particles; ρ_w is the density of water; θ is the bed slope. If suspension of particles is not considered, the yield stress at limit equilibrium can be calculated using the Mohr–Coulomb equation:

$$\tau_y = C_v(\rho_s - \rho_w)gh\cos^2\theta\tan\phi, \quad (15)$$

where ϕ is the friction angle of the solid particles contacting the bed. The effective cohesion of the debris flow material is taken as zero in the above equation. If only the particles in contact are considered, the yield stress can be calculated by incorporating a coefficient of suspension of solid particles as follows:

$$\tau_y = (1 - C_s)C_v(\rho_s - \rho_w)gh\cos^2\theta\tan\phi, \quad (16)$$

where C_s is the coefficient of suspension of solid particles and $(1 - C_s)$ represents the portion of solid particles that are in contact.

GMDD
7, 7267–7316, 2014

Three typical suspension scenarios are shown in Fig. 5: partial suspension, $0 < C_s < 1$; full suspension, $C_s = 1$; and no suspension, $C_s = 0$. The three scenarios have the same volumetric sediment concentration but different C_s values. C_s is in the range between 0 and 1 in most cases, which means that the solid particles are partially suspended (Fig. 5a). C_s is 1 when all the solid particles are suspended and do not contact with the bed (Fig. 5b); C_s is 0 when all the solid particles are retained on the bed and no suspension occurs (Fig. 5c). In reality, part of the solid particles are in suspension due to buoyant forces, collision between solid particles, and turbulent fluid forces. The value of C_s is related to particle size and flow discharge. A smaller particle size gives a larger C_s value since smaller particles are more likely to suspend in water. Larger flow discharges also give larger C_s values based on field observations (Alexandrov et al., 2003).

The values of C_v in most laboratory tests range between 0.1 and 0.8 (e.g. O'Brien and Julien, 1988; Coussot et al., 1998; Schatzmann et al., 2009; Sosio and Crosta, 2009; Bisantino et al., 2010) and Eq. (12) can be adopted to estimate μ when C_v is greater than or equal to 0.1. When C_v is smaller than 0.1, Eq. (12) is not valid and μ is assumed to increase linearly from 0.001 Pa s for water to $\alpha_1 \, e^{0.1\beta 1}$.

2.4 Erosion and deposition

Erosion occurs when the bed shear stress is sufficiently large and the volumetric sediment concentration is smaller than an equilibrium value. The equilibrium value proposed by Takahashi et al. (1992) is adopted in this study:

$$C_{v\infty} = \frac{\rho_w \tan\theta}{(\rho_s - \rho_w)(\tan\phi_{bed} - \tan\theta)}, \quad (17)$$

where $C_{v\infty}$ is the equilibrium volumetric sediment concentration; ϕ_{bed} is the internal friction angle of the erodible bed. The computed $C_{v\infty}$ value is larger than 1 when θ approaches ϕ_{bed}, and smaller than 0 when θ is larger than ϕ_{bed}, both indicating an

GMDD
7, 7267–7316, 2014

unstable or quasi-stable bed. Solid materials are difficult to be retained on such a steep slope. Hence, no erosion is expected to occur on such a slope.

The erosion rate can be described approximately by the following equation:

$$i = K_e(\tau - \tau_c), \tag{18}$$

where i is the erosion rate; K_e is the coefficient of erodibility, which is a soil property that describes the erosion speed; τ is the shear stress; τ_c is the critical erosive shear stress. The shear stress (Hanson, 1990) can be computed as follows:

$$\tau = \rho g h S_f. \tag{19}$$

The critical erosive shear stress can be calculated by considering the partly suspended particles at limit equilibrium using the Mohr–Coulomb equation:

$$\tau_c = c' + (1 - C_s)C_v(\rho_s - \rho_w)gh\cos^2\theta\tan\phi_{bed}, \tag{20}$$

where c' is the effective cohesion of the bed material. Based on Eqs. (17)–(20), erosion occurs if τ is larger than τ_c and C_v is smaller than $C_{v\infty}$ (Fig. 1). K_e and τ_c can also be measured in-situ using a jet index method (e.g. Chang et al., 2011).

When the debris flow moves to a flatter place, deposition occurs if C_v is larger than the respective $C_{v\infty}$ value (Fig. 1) and the flow velocity is smaller than a critical value. Takahashi et al. (1992) proposed the following critical flow velocity for the initiation of deposition:

$$V_e = \frac{2}{5d_{50}}\left(\frac{g\sin\theta_e\rho}{0.02\rho_s}\right)^{0.5}\lambda^{-1}h^{1.5}, \tag{21}$$

where

$$\tan\theta_e = \frac{C_v(\rho_s - \rho_w)\tan\phi_{bed}}{C_v(\rho_s - \rho_w) + \rho_w}, \tag{22}$$

$$\lambda^{-1} = \left(\frac{C_{v*}}{C_v}\right)^{\frac{1}{3}} - 1, \tag{23}$$

GMDD
7, 7267–7316, 2014

ρ is the density of debris flow and can be computed as follows:

$$\rho = C_v(\rho_s - \rho_w) + \rho_w, \tag{24}$$

where d_{50} is the mean particle size of the debris flow mixture. The deposition rate can be expressed as follows (Takahashi et al., 1992):

$$i = \delta_d \left(1 - \frac{V}{pV_e}\right) \frac{C_{v\infty} - C_v}{C_{v*}} V, \tag{25}$$

where δ_d is a coefficient that describes the deposition rate; p (< 1) is a coefficient introduced to account for the difference between the locations where actual deposition takes place in the experiment and where the velocity becomes less than V_e (Takahashi et al., 1992).

2.5 Numerical solution algorithm

The analysis domain is discretized into a grid first, with properties of each cell assigned, including the initial flow depth, the thickness and properties of the erodible soil layer, the elevation of the non-erodible layer, Manning's coefficient and so on. The directions of a debris flow are multiple. Although the governing equation is in a one-dimensional form, the model can simulate flows in multi-directions. In this model, a one-dimensional governing equation and eight flow directions are adopted, which have been proven to be sufficient and efficient for simulating overland flows (FLO-2D Software Inc., 2009).

As shown in Fig. 4, each cell has eight flow directions; namely, four compass directions (i.e. north, east, south and west) and four diagonal directions (i.e. northeast, southeast, southwest and northwest). In each time step, the flow velocity and flow discharge across each flow boundary (i.e. Γ_N, Γ_E, Γ_S, Γ_W, Γ_{NE}, Γ_{SE}, Γ_{SW}, Γ_{NW} in Fig. 4) are computed. The change in the flow depth at the cell is evaluated. The calculation is conducted cell by cell. For each center cell, the calculation is conducted between the

GMDD
7, 7267–7316, 2014
EDDA

H. X. Chen and
L. M. Zhang

center cell and each of the eight adjacent cells separately (Fig. 4). An efficient numerical solution algorithm is developed for this model, which is introduced step by step as follows:

1. At the beginning of each time step, the erosion rate or deposition rate is computed for each cell. The flow depth and volumetric sediment concentration of each cell are updated using Eqs. (1) and (2) as follows:

$$h_{\text{predi}} = h^n + \{i[C_{\text{v}*} + (1 - C_{\text{v}*})s_{\text{b}}]\}\,\Delta t, \tag{26}$$

$$C_{\text{vpredi}} = \frac{\left(C_{\text{v}}^n h^n + iC_{\text{v}*}\Delta t\right)}{h_{\text{predi}}}, \tag{27}$$

where superscript n notes the sequence of time stepping. The spatial differences of hv and $C_{\text{v}}hv$ in Eqs. (1) and (2) are not considered at this stage but will be accounted for in step 4. The updated bed elevation and density of flow, ρ_{predi}, can be computed using Eqs. (4) and (24), respectively.

2. The average flow depth, flow density, volumetric sediment concentration and roughness of the two cells (i.e. the center cell and one of the eight adjacent cells) are computed. The bed slope between the two cells is defined using the gradient between the centers of the cells.

3. The new flow velocity across each flow boundary is obtained by solving Eq. (3):

$$v_{\text{predi}} = v^n + \left\{ g\left[-\text{sgn}(v)S_{\text{f}} - \frac{\partial(z_{\text{b}} + h_{\text{predi}})}{\partial x}\right] - \frac{v^n i[C_{\text{v}*} + (1 - C_{\text{v}*})s_{\text{b}}]}{h_{\text{predi}}} - v^n\frac{\partial v^n}{\partial x}\right\}\Delta t. \tag{28}$$

GMDD
7, 7267–7316, 2014

4. The discharge, q, across the flow boundaries is then computed, and the flow depth and density are updated as follows:

$$h_{\text{new}} = h_{\text{predi}} + \frac{(q_E + q_{\text{SE}} + q_S + q_{\text{SW}} + q_W + q_{\text{NW}} + q_N + q_{\text{NE}})\Delta t}{A_{\text{cell}}}, \tag{29}$$

$$\rho_{\text{new}} = \frac{h_{\text{predi}}\rho_{\text{predi}}A_{\text{cell}} + (\rho_E q_E + \rho_{\text{SE}} q_{\text{SE}} + \rho_S q_S + \rho_{\text{SW}} q_{\text{SW}} + \rho_W q_W + \rho_{\text{NW}} q_{\text{NW}} + \rho_N q_N + \rho_{\text{NE}} q_{\text{NE}})\Delta t}{h_{\text{new}} A_{\text{cell}}}, \tag{30}$$

where h_{new} and ρ_{new} are the updated flow depth and density, respectively; q_{E} and ρ_{E} are the discharge and density of exchange flow across the east boundary, respectively (and so on for other directions); A_{cell} is the area of the cell. By considering the changes of flow and density due to the flow between any two cells, the influence of the spatial differences of hv and $C_{\text{v}}hv$ that are not considered in step 1 is considered in this step.

5. To make the solution more robust, the average values of v^n and v_{predi} are computed and steps (1)–(4) are repeated until the value of v_{predi} converges. Once this is achieved, the values of v_{predi}, h_{new} and ρ_{new} are assigned to v^{n+1}, h^{n+1} and ρ^{n+1}, respectively, and the time step moves forward.

2.6 Time stepping and numerical stability

On one hand, the time step should be sufficiently small to ensure the numerical stability. On the other hand, the time step should be large enough to attain reasonable computation efficiency. A variable time scheme is adopted in this research to ensure both the numerical stability and the computation efficiency, especially for cases which involve a large number of cells so that the simulation time is likely long. The algorithm for the variable time stepping scheme is shown in Fig. 6.

GMDD
7, 7267–7316, 2014

Three convergence criteria are adopted in this study. The first criterion is the Courant–Friedrich–Lewy (CFL) condition; namely, a particle of fluid should not travel more than the cell size in one time step, Δt. The second criterion states that the percent change of flow depth in one time step should not exceed a specified tolerant value, TOLP(h) (e.g. 10 %), which ensures that the flow depth at one cell will not change from a positive value to a negative value within one time step. If the flow moves to a cell with a zero flow depth, the second criterion cannot be satisfied and the third criterion is needed. The third criterion states that the change of flow depth in one time step should not exceed a specified tolerant value, TOL(h) (e.g. 0.1 m), which makes the time step move forward even though the second criterion cannot be satisfied. The values of TOLP(h) and TOL(h) depend on required accuracy and the maximum flow depth. Larger values of TOLP(h) and TOL(h) lead to higher computation efficiency but lower accuracy. Hence, if the first criterion and either one of the last two criteria are satisfied for all cells, the time step can move forward successfully, and the time step can be enlarged. Otherwise, the computation for that time step must be abandoned and the time step should be shortened until the required criteria are satisfied.

3 Model verification

In this section, four numerical tests are conducted to verify the performance of the proposed model. In Test 1, an analytical solution to one-dimensional dam-break water flow is adopted to validate the performance of the numerical solution algorithm. In Test 2, an analytical solution to one-dimensional debris flow is adopted to validate the performance of the model in simulating the movement of a debris flow with constant material properties. In Test 3, a flume test is adopted to validate the performance of the model in describing the erosion process and material property changes. In Test 4, another flume test is adopted to validate the performance of the model in describing the movement of a debris flow considering the material property changes due to both erosion and deposition.

GMDD
7, 7267–7316, 2014

3.1 Test 1: analytical solution to one-dimensional dam-break water flow

Flow in a wide, horizontal, rectangular, and frictionless channel reported by Fennema and Hanif Chaudhry (1987) is adopted. The problem is described in Fig. 7. A dam in a channel is instantaneously removed across its entire width at time $t = 0$ and the flow conditions are computed up to time $t = 60$ s after removing the dam. A 2000 m long channel is simulated, which is subdivided into 400 equal-length reaches and the cell size is 5 m. The time step is kept at 0.001 s. The flow resistance slope, S_f, is taken as 0 in this test as the channel is assumed frictionless. Since the problem is one-dimensional, there are only two flow directions and two flow boundaries for each cell. The width of the flow boundary equals the cell size. The water surface elevations from the analytical solution of Fennema and Hanif Chaudhry (1987) and the numerical solution at $t = 60$ s are compared in Fig. 8. The computed flow velocity between $x = 700$ and 1500 m is 2.85 m s^{-1}, and the value from the analytical solution is 2.92 m s^{-1}. The error is only 2.4 %. Hence, the model simulates very well the one-dimensional dam-break water flow problem.

3.2 Test 2: analytical solution to one-dimensional debris flow with constant properties

The problem described by Liu and Mei (1989) is adopted in this test. The materials are initially retained as a triangular pile by a board and the initial profile is shown in Fig. 9. The materials start moving after the board is removed and cease moving finally due to the presence of yield stress. The final profile for the one-dimensional flow is (Liu and Mei, 1989)

$$h^2 = \pm\frac{2\tau_y}{\rho g}x + a^2, \tag{31}$$

where a is a coefficient; ρ and μ are 1200 kg m^{-3} and 5 Pa s, respectively (Liu and Mei, 1989). Given an a value of 0.5 m, τ_y is 475 Pa (Liu and Huang, 2006). The bottom

GMDD
7, 7267–7316, 2014

surface is assumed to be smooth and the Manning coefficient is hence 0. The resistance parameter for laminar flow, K, is set to be 2500 after several trial computations. The cell size is set to be 0.1 m following Liu and Huang (2006). The final profiles from the analytical solution and the numerical solution are compared in Fig. 9. The maximum error is only 1 %. The model simulates the movement of the debris flow exceptionally well.

3.3 Test 3: flume test considering changes in debris flow properties due to erosion

A series of flume experiments conducted by Takahashi et al. (1992) is simulated in this test. The width of the flume was 10 cm. Four experiments with different lengths of erodible bed layer (L = 1, 2, 3, 4 m) were conducted. The thickness of the erodible bed layer was 10 cm. The slope of the flume was maintained at 18°. A partition and a sampler were installed at the outlet of the flume. Figure 10 shows the experiment setup for L = 4 m. The mean particle size, d_{50}, of the bed material was 1.66 mm, and the C_{v*} value was 0.655. During the test, water was applied from the upstream end with a constant discharge of 2000 $cm^3 s^{-1}$ to produce debris flow. The measured values of the volumetric sediment concentration, C_v, at the debris flow front when the debris flow front moved 1, 2, 3 and 4 m were 0.25, 0.40, 0.39, 0.40, respectively.

In the simulation, the flume is discretized into a grid with cell dimensions of 0.05 m × 0.05 m. No flow is allowed across the flume walls. The soil properties and hydrological parameters used to simulate the debris flow considering the erosion process in this test are summarized in Tables 1 and 2, respectively. Some parameters are adopted from Takahashi et al. (1992); namely, c', d_{50}, ρ_w, ρ_s, ϕ, ϕ_{bed}, s_b, C_{v*}. The values of α_1 and β_1 for computing the dynamic viscosity are adopted from Bisantino et al. (2010). The mean particle size of the samples in the tests of Bisantino et al. (2010) ranged from 0.6 to 0.9 mm, which was close to the value of the materials used in the flume tests by Takahashi et al. (1992). The resistance parameter for laminar flow, K, is determined as 500, which is within the recommended range for erodible sand surfaces

GMDD
7, 7267–7316, 2014

(FLO-2D Software Inc., 2009). The Manning coefficient is estimated to be 0.10, which is within the recommended range for open grounds with debris (FLO-2D Software Inc., 2009). The values of C_s and K_e are determined based on several trial calculations. The time step is kept at 0.002 s. The calculated C_v values when the debris flow front moves 1, 2, 3 and 4 m are 0.25, 0.39, 0.45, 0.46, respectively. The errors when compared with the measured values are 0, 2.5, 15.4, and 15 %, respectively. The model reproduces the erosion process reasonably well.

3.4 Test 4: flume test considering changes in debris flow properties due to erosion and deposition

Another series of flume tests conducted by Takahashi et al. (1992) is adopted in Test 4. The experiment setup is shown in Fig. 11. In the test series, the flume width was also 10 cm. The bed layer had a length of 3.0 m and a thickness of 10 cm, which was located 5.5 m from the outlet of the flume. A partition with a height of 10 cm was used to retain the sediment. A board inclined at 5° longitudinally (Fig. 11b) was connected to the outlet to observe the temporal variations of the shape and elevations of the debris fan. The mean particle size, d_{50}, of the bed material was 3.08 mm, and the C_{v*} value was 0.65. The surface of the bed was glued with the same material to increase the roughness. Water was later applied from the upstream end at a constant discharge of 600 $cm^3 s^{-1}$ for 20 s to produce debris flow. To consider the uncertainties of the sample properties, the tests were conducted six times repeatedly. In each run, the discharge at the outlet of the flume was measured. The first two runs are treated as trial runs in this study, and the results of the last four runs are adopted for comparison.

In the simulation, the flume is discretized into a grid with cell dimensions of 0.05 m × 0.05 m. No flow is allowed across the flume walls. Various time steps are adopted in this test following the algorithm in Fig. 6, with a minimum time step of 0.001 s, a maximum converging time step of 0.005 s, Δt_I of 0.0005 s, Δt_D of 0.001 s, TOLP(h) of 2 %, and TOL(h) of 0.5 cm. The soil properties and hydrological parameters used to simulate the erosion and deposition processes are summarized in Tables 1

GMDD
7, 7267–7316, 2014

and 2, respectively, which are obtained following the same methods in Test 3. Takahashi et al. (1992) found that the erosion rate was inversely proportional to the mean particle size. Since the mean particle size in Test 4 was nearly twice of that in Test 3, the coefficient of erodibility, K_e, is therefore taken as one half of that in Test 3. The Manning coefficient is determined as 0.1 for the flume covered by the saturated sand and 0.05 for the other parts, which are within the recommended range for open grounds without debris (FLO-2D Software Inc., 2009). The coefficient of deposition rate, δ_d, is determined as 0.01 after trial calculations.

The computed discharges at the outlet and the measured results from the last four experiments are compared in Fig. 12. Time $t = 0$ in Fig. 12 denotes the time when the debris flow front reaches the outlet. As shown in Fig. 12, the model describes very well the movement of the debris flow in the confined channel.

When the debris flow moves to the flood board (Fig. 11), it decelerates and deposits gradually. The debris fan in the experimental tests and numerical solution are compared in Fig. 13. The contours mean the thickness of the debris fan. The thickness of the debris fan is the sum of the flow depth and the deposit thickness before the flow stops; and is the deposit thickness after the flow stops. At $t = 5$ s after the debris flow runs out of the outlet, the calculated runout distance of the debris fan (60 cm) is slightly smaller than the experimental result (70 cm) while the calculated width of the debris fan (70 cm) is slightly larger than the experimental result (50 cm). At $t = 10$ s after the debris flow runs out, the calculated runout distance of the debris fan (90 cm) is almost the same as the experimental result. The calculated width of the debris fan (85 cm) is slightly larger than the experimental result (65 cm). At the final stage, the calculated runout distance (105 cm) is slightly larger than the experimental result (100 cm); and the calculated width of the debris fan (90 cm) is slightly larger than the experimental result (80 cm). The calculated debris thickness distributions on the debris fans at the three moments also match the respective experimental results reasonably well. Hence, the model also describes well the movement of debris flows in the unconfined flat area.

GMDD
7, 7267–7316, 2014
EDDA

H. X. Chen and
L. M. Zhang

4 Field application

4.1 Xiaojiagou debris flow event on 14 August 2010

Rainfall-induced landslides are one of the most catastrophic hazards in mountainous areas (e.g. Chen and Zhang, 2014; Chen et al., 2012; Raia et al., 2014). Decisions for effective risk mitigation require hydrological and landslide analysis at the regional scale (e.g. O'Brien et al., 1993; Formetta et al., 2011; Archfield et al., 2013; Chen et al., 2013). The 2008 Wenchuan earthquake triggered numerous landslides, leaving a large amount of loose materials on the hill slopes or channels. From 12 August 2010 to 14 August 2010, a storm swept the epicenter, Yingxiu, and its vicinity, triggering a catastrophic debris flow in Xiaojiagou Ravine (Fig. 14). About 1.01×10^6 m^3 of deposit was brought out in the form of a channelized debris flow. According to the rainfall record at Yingxiu that is 5 km from Xiaojiagou Ravine, the total rainfall amount was 220 mm in a period of 40 h (Chen et al., 2012). The debris flow was witnessed to occur at the ravine mouth at about 5 a.m. on 14 August (i.e. 36 h after the storm started) and lasted about 30 min. The cumulative rainfall from the beginning of the storm to the occurrence of the debris flow was 188 mm. The runout materials of the debris flow buried 1100 m of road, blocked the Yuzixi River, formed a debris flow barrier lake and raised the river bed by at least 15 m.

Interpretation of the satellite images taken before and after the debris flow reveals that the source material of this debris flow was mainly the channel colluvium (Chen et al., 2012). The deposits in the main channel marked "location of the main source material" in Figs. 14 and 15 had a volume of approximately 0.74×10^6 m^3 before the debris flow event and much of it had been washed away (Chen et al., 2012). Based on interpretation of satellite images and field investigations, the observed deposition zone is determined and shown in Fig. 14.

GMDD
7, 7267–7316, 2014

H. X. Chen and
L. M. Zhang

4.2 Determination of input information

The study area is divided into two domains, one for rainfall–runoff simulation and the other for debris flow runout simulation (Fig. 15). Grid systems are created within the two domains with grid sizes of 30 m × 30 m for domain one and 15 m × 15 m for domain two. After the debris flow, detailed field investigations and laboratory tests were conducted. The hydrological parameters for rainfall runoff simulation and debris flow runout simulation have been proposed by Chen et al. (2013) and are summarized in Table 3.

Rainfall runoff simulation is conducted first in domain one using FLO-2D (FLO-2D Software Inc., 2009). The rainfall data at Yingxiu is adopted. The runoff water would be retained by the colluvium and accumulate behind the landslide deposits, forming landslide barrier ponds. The cumulative runoff water at Sect. 1-1 (Figs. 14 and 15) can be computed, which is applied at Sect. 1-1 as the inflow hydrograph for debris flow runout simulation in domain two. Debris flow would occur when the barrier ponds breach. The source materials are assumed to be saturated before the occurrence of debris flow. As water flows over the source material, erosion occurs if the conditions in Eqs. (17)–(20) are met. Since the debris flow was witnessed to occur at the ravine mouth about 36 h after the storm started and lasted about 30 min, the cumulative runoff water at Sect. 1-1 in Fig. 14 at 36 h after the storm started is adopted to create the inflow hydrograph, and the surface runoff is determined to be $0.5 \times 10^6\ m^3$. For simplicity, the inflow hydrograph is assumed to be an isosceles triangle (Fig. 16). The duration and the peak discharge are 0.5 h and $556\ m^3\ s^{-1}$, respectively. The area of the inflow hydrograph is equal to $0.5 \times 10^6\ m^3$.

In domain two, the source material is distributed into 329 cells with a thickness of 10 m. The internal friction angle, ϕ_{bed}, for the source material is determined as 37° according to the test results of Zhao et al. (2013). Since the source material has a very low content of silt and clay (< 2 %) according to sieving tests (Chen et al., 2012), the true cohesion, c', is assumed to be 0 in the debris flow runout simulation. The values of d_{50}, ρ_s, C_{v*} are determined based on field and laboratory sieving tests. The

GMDD
7, 7267–7316, 2014
EDDA

H. X. Chen and
L. M. Zhang

method and testing results have been reported in detail by Chen et al. (2012). Since the source material is assumed to be saturated, s_b is 1. K_e is determined using an empirical equation developed based on field tests in the Wenchuan earthquake zone by Chang et al. (2011):

$$K_e = 0.020075 e^{4.77} C_u^{-0.76}, \quad (32)$$

where e is the void ratio and C_u is the coefficient of uniformity. The values of e and C_u are 0.54 and 39, respectively, based on the sieving tests. Hence, K_e is 6.6×10^{-5} m^3/(Ns). The soil properties are summarized in Table 1. The values of α_1, β_1, K, and n are determined following Chen et al. (2013). The value of C_s and δ_d are determined after several trial computations. The hydrological parameters for simulating the erosion and deposition processes are summarized in Table 2. Various time steps are adopted in this test following the algorithm in Fig. 6, with a minimum time step of 0.01 s, a maximum converging time step of 1.0 s, Δt_I of 0.01 s, Δt_D of 0.02 s, TOLP(h) of 20 %, and TOL(h) of 0.5 m.

4.3 Changes in debris flow properties during the flow process

The values of the volumetric sediment concentration, C_v, when the debris flow reaches Sects. 1-1, 2-2, 3-3, 4-4 in Fig. 14 are computed, which are 0, 0.13, 0.23, 0.49, respectively. With the increase of C_v, the yield stress and dynamic viscosity also increase significantly as Fig. 3 shows.

The change of C_v with time at Sect. 3-3 is shown in Fig. 17. C_v is 0.23 at $T = 0$ when the forefront reaches the section, which can be viewed as the precursory surge in Fig. 1. Afterwards, C_v increases very quickly to a peak value of about 0.5, which can be viewed as the boulder front in Fig. 1. After the boulder front passes, C_v sustains at the peak value for some time (about 60 s), which can be viewed as the steady flow region in Fig. 1. After that, C_v decreases gradually to a lower level, which can be viewed as the hyper-concentrated flow in Fig. 1. This flow region is erosive and the bedding

GMDD
7, 7267–7316, 2014
EDDA

H. X. Chen and
L. M. Zhang

solid materials can be entrained. The erosion process upstream Sect. 3-3 lasts about 300 s.

4.4 Comparison between simulated and observed results

The volume of the simulated debris flow is about 1.0×10^6 m^3. Since the sum of inflow water (0.5×10^6 m^3) and the saturated source material (0.74×10^6 m^3) is 1.24×10^6 m^3, approximately 0.24×10^6 m^3 of source material is not entrained into the debris flow in the simulation. Hence, not all the source material erodes.

The simulated and observed deposition zones are shown in Fig. 18a. The simulated inundated area and runout distance match the observed results reasonably well. It is noted that the depth at the debris fan front is significantly smaller, which is the precursory surge in Fig. 1. The distribution of the maximum flow velocity is shown in Fig. 18b, which indicates that the debris flow moves very rapidly, especially in the ravine channel. Taking into account the large volume, the debris flow is very destructive, which has been observed by Chen et al. (2012).

The comparison between the simulation results and the observations suggests that the model evaluates well the volume of debris flow considering the erosion process. The inundated area and the runout distance can also be predicted reasonably well.

5 Limitations of the proposed method

The mathematical model proposed in this study has limitations due to the simplifying assumptions and approximations in the underlying theory. The main limitations are as follows:

1. The flow velocity in each of the eight flow directions is computed independently, which does not consider the flow velocity gradient with respect to the orthogonal direction (Eq. 3). The influence is not significant in a confined channel since the orthogonal gradient is normally small. In an unconfined flat area, the eight flow

GMDD
7, 7267–7316, 2014
EDDA
H. X. Chen and L. M. Zhang

directions account for the influence to some extent, but further work is needed to test the performance of the model.

2. The governing equations are in a depth-integrated form, hence the particle segregation in the vertical direction cannot be considered.

3. A hydrostatic pressure distribution is assumed along the vertical direction. The assumption influences the computed yield stress, which may in turn affect the runout characteristics.

4. The suspension coefficient, C_s, can vary with mean particle size and discharge. In Tests 3 and 4, C_s is assumed to be a constant for simplicity. Further work is desired to properly determine this parameter.

6 Summary and conclusions

A new depth-integrated numerical model for simulating debris flow erosion, deposition, and property changes (EDDA) is developed in this study. The model considers the changes in debris flow density, yield stress, and dynamic viscosity, as well as the influences of such changes on the runout characteristics of the debris flow.

The model is unique in that it considers erosion and deposition processes, and changes in debris flow mass, debris flow properties and topography due to erosion and deposition. Considering the partly suspended solid particles at limit equilibrium, the yield stress of the debris flow mixture is estimated using the Mohr–Coulomb equation, which is suitable for any of clear water flow, hyper-concentrated flow, and fully developed debris flow. A variable time step algorithm is developed to assure both numerical stability and computation efficiency. Although the governing equations are in a one-dimensional depth-integrated form, the model describes well flows in multi-directions.

Four numerical tests have been conducted to verify the performance of the model. In Tests 1 and 2, analytical solutions to one-dimensional dam-break water flow and

GMDD
7, 7267–7316, 2014

H. X. Chen and
L. M. Zhang

debris flow are adopted, respectively. Comparisons between the numerical solutions and the analytical solutions indicate that the model simulates exceptionally well the one-dimensional dam-break water flow and the one-dimensional movement of debris flow with constant properties. Flume tests are adopted in Tests 3 and 4. The calculated volumetric sediment concentration at the debris flow front agrees with the experimental results very well in Test 3. In Test 4, the model simulates reasonably well the erosion and deposition processes, and the movement of the multi-direction debris flows in the confined channel and the unconfined flat area in terms of the discharge hydrographs at the outlet and the time-varying geometery and elevations of the debris fan.

The model is also applied to simulate a large-scale debris flow in Xiaojiagou Ravine to test the performance of the model in catchment-scale simulations. The model well describes the changes in debris flow properties and estimates the volume of debris flow. Considering the deposition process, the inundated area and the runout distance are predicted properly. The model is a powerful tool for debris flow risk assessment in a large area and is intended for use as a module in a real-time warning system for debris flows.

Acknowledgements. This research was substantially supported by Sichuan Department of Transportation and Communications, the Natural Science Foundation of China (Grant No. 51129902), and the Research Grants Council of Hong Kong (No. 16212514).

References

Alexandrov, Y., Laronne, J. B., and Reid, I.: Suspended sediment concentration and its variation with water discharge in a dryland ephemeral channel, northern Negev, Israel, J. Arid Environ., 53, 73–84, 2003.

Archfield, S. A., Steeves, P. A., Guthrie, J. D., and Ries III, K. G.: Towards a publicly available, map-based regional software tool to estimate unregulated daily streamflow at ungauged rivers, Geosci. Model Dev., 6, 101–115, doi:10.5194/gmd-6-101-2013, 2013.

GMDD
7, 7267–7316, 2014

Bartelt, P., Buehler, Y., Christen, M., Deubelbeiss, Y., Graf, C., McArdell, B., Salz, M., and Schneider, M.: A Numerical Model for Debris Flow in Research and Practice, User Manual v1.5 Debris Flow, WSL Institute for Snow and Avalanche Research SLF, 2013.
Beguería, S., Van Asch, Th. W. J., Malet, J.-P., and Gröndahl, S.: A GIS-based numerical model for simulating the kinematics of mud and debris flows over complex terrain, Nat. Hazards Earth Syst. Sci., 9, 1897–1909, doi:10.5194/nhess-9-1897-2009, 2009.
Berger, C., McArdell, B. W., Fritschi, B., and Schlunegger, F.: A novel method for measuring the timing of bed erosion during debris flows and floods, Water Resour. Res., 46, W02502, doi:10.1029/2009WR007993, 2010.
Bisantino, T., Fischer, P., and Gentile, F.: Rheological characteristics of debris-flow material in South-Gargano watersheds, Nat. Hazards, 54, 209–223, 2010.
Boss Corporation: DAMBRK – User's Manual, Boss International Inc., Madison, WI, USA, 1989.
Cannon, S. H. and Savage, W. Z.: A mass change model for the estimation of debris flow runout, J. Geol., 96, 221–227, 1988.
Chang, D. S., Zhang, L. M., Xu, Y., and Huang, R. Q.: Field testing of erodibility of two landslide dams triggered by the 12 May Wenchuan earthquake, Landslides, 8, 321–332, 2011.
Chen, H., Crosta, G. B., and Lee, C. F.: Erosional effects on runout of fast landslides, debris flows and avalanches: a numerical investigation, Geotechnique, 56, 305–322, 2006.
Chen, H. X. and Zhang, L. M.: A physically-based distributed cell model for predicting regional rainfall-induced shallow slope failures, Eng. Geol., 176, 79–92, 2014.
Chen, H. X., Zhang, L. M., Chang, D. S., and Zhang, S.: Mechanisms and runout characteristics of the rainfall-triggered debris flow in Xiaojiagou in Sichuan Province, China, Nat. Hazards, 62, 1037–1057, 2012.
Chen, H. X., Zhang, L. M., Zhang, S., Xiang, B., and Wang, X. F.: Hybrid simulation of the initiation and runout characteristics of a catastrophic debris flow, J. Mt. Sci., 10, 219–232, 2013.
Chen, H. X., Zhang, L. M., and Zhang, S.: Evolution of debris flow properties and physical interactions in debris-flow mixtures in the Wenchuan earthquake zone, Eng. Geol., online first, doi:10.1016/j.enggeo.2014.08.004, 2014.
Coussot, P., Laigle, D., Arattano, M., Deganutti, A., and Marchi, L.: Direct determination of rheological characteristics of debris flow, J. Hydraul. Eng., 124, 865–868, 1998.

GMDD
7, 7267–7316, 2014

Crosta, G. B., Imposimato, S., and Roddeman, D. G.: Numerical modelling of large landslides stability and runout, Nat. Hazards Earth Syst. Sci., 3, 523–538, doi:10.5194/nhess-3-523-2003, 2003.
Denlinger, R. P. and Iverson, R. M.: Flow of variably fluidized granular masses across three-dimensional terrain: 2. Numerical predictions and experimental tests, J. Geophys. Res.-Sol. Ea., 106, 553–566, 2001.
Egashira, S., Honda, N., and Itoh, T.: Experimental study on the entrainment of bed material into debris flow, Phys. Chem. Earth Pt. C, 26, 645–650, 2001.
Fennema, R. J. and Hanif Chaudhry, M.: Simulation of one-dimensional dam-break flows, J. Hydraul. Res., 25, 41–51, 1987.
FLO-2D Software Inc.: FLO-2D Reference Manual, Nutrioso, AZ, USA, 2009.
Formetta, G., Mantilla, R., Franceschi, S., Antonello, A., and Rigon, R.: The JGrass-NewAge system for forecasting and managing the hydrological budgets at the basin scale: models of flow generation and propagation/routing, Geosci. Model Dev., 4, 943–955, doi:10.5194/gmd-4-943-2011, 2011.
Fraccarollo, L. and Papa, M.: Numerical simulation of real debris-flow events, Phys. Chem. Earth Pt. B, 25, 757–763, 2000.
Ghilardi, P., Natale, L., and Savi, F.: Modeling debris flow propagation and deposition, Phys. Chem. Earth Pt. C, 26, 651–656, 2001.
Hanson, G. J.: Surface erodibility of earthen channels at high stresses part I-open channel testing, T. ASAE, 33, 127–131, 1990.
Hungr, O.: A model for the runout analysis of rapid flow slides, debris flows, and avalanches, Can. Geotech. J., 32, 610–623, 1995.
Hungr, O. and McDougall, S.: Two numerical models for landslide dynamic analysis, Comput. Geosci., 35, 978–992, 2009.
Hungr, O., McDougall, S., and Bovis, M.: Entrainment of material by debris flows, in: Debris-Flow Hazards and Related Phenomena, edited by: Jakob, M. and Hungr, O., Springer-Praxis, Chichester, UK, 135–158, 2005.
Iverson, R. M.: Elementary theory of bed-sediment entrainment by debris flows and avalanches, J. Geophys. Res.-Earth, 117, F03006, doi:10.1029/2011JF002189, 2012.
Julien, P. Y. and Lan, Y.: Rheology of hyperconcentrations, J. Hydraul. Eng., 117, 346–353, 1991.

GMDD
7, 7267–7316, 2014

Kwan, J. S. and Sun, H. W.: An improved landslide mobility model, Can. Geotech. J., 43, 531–539, 2006.
Li, W. C., Li, H. J., Dai, F. C., and Lee, L. M.: Discrete element modeling of a rainfall-induced flowslide, Eng. Geol., 149, 22–34, 2012.
Liu, K. F. and Huang, M. C.: Numerical simulation of debris flow with application on hazard area mapping, Comput. Geosci., 10, 221–240, 2006.
Liu, K. F. and Mei, C. C.: Slow spreading of a sheet of Bingham fluid on an inclined plane, J. Fluid Mech., 207, 505–529, 1989.
Major, J. J. and Pierson, T. C.: Debris flow rheology: experimental analysis of fine-grained slurries, Water Resour. Res., 28, 841–857, 1992.
Medina, V., Hürlimann, M., and Bateman, A.: Application of FLATModel, a 2-D finite volume code, to debris flows in the northeastern part of the Iberian Peninsula, Landslides, 5, 127–142, 2008.
O'Brien, J. S. and Julien, P. Y.: Laboratory analysis of mudflow properties, J. Hydraul. Eng., 114, 877–887, 1988.
O'Brien, J. S., Julien, P. Y., and Fullerton, W. T.: Two-dimensional water flood and mudflow simulation, J. Hydraul. Eng., 119, 244–261, 1993.
Pastor, M., Haddad, B., Sorbino, G., Cuomo, S., and Drempetic, V.: A depth-integrated, coupled SPH model for flow-like landslides and related phenomena, Int. J. Numer. Anal. Met., 33, 143–172, 2009.
Pierson, T. C. and Scott, K. M.: Downstream dilution of a lahar: transition from debris flow to hyperconcentrated streamflow, Water Resour. Res., 21, 1511–1524, 1985.
Raia, S., Alvioli, M., Rossi, M., Baum, R. L., Godt, J. W., and Guzzetti, F.: Improving predictive power of physically based rainfall-induced shallow landslide models: a probabilistic approach, Geosci. Model Dev., 7, 495–514, doi:10.5194/gmd-7-495-2014, 2014.
Rickenmann, D.: Hyperconcentrated flow and sediment transport at steep slopes, J. Hydraul. Eng., 117, 1419–1439, 1991.
Schatzmann, M., Bezzola, G. R., Minor, H. E., Windhab, E. J., and Fischer, P.: Rheometry for large-particulated fluids: analysis of the ball measuring system and comparison to debris flow rheometry, Rheol. Acta, 48, 715–733, 2009.
Sosio, R. and Crosta, G. B.: Rheology of concentrated granular suspensions and possible implications for debris flow modeling, Water Resour. Res., 45, W03412, doi:10.1029/2008WR006920, 2009.

GMDD
7, 7267–7316, 2014

Takahashi, T.: Debris Flow: Mechanics, Prediction and Countermeasures, Taylor & Francis, 2007.
Takahashi, T., Nakagawa, H., Harada, T., and Yamashiki, Y.: Routing debris flows with particle segregation, J. Hydraul. Eng., 118, 1490–1507, 1992.
van Asch, Th. W. J., Tang, C., Alkema, C., Zhu, J., and Zhou, W.: An integrated model to assess critical rainfall thresholds for run-out distances of debris flows, Nat. Hazards, 70, 299–311, 2014.
Voellmy, A.: Uber die Zerstorungskraft von Lawinen, Schweizerische Bauzeitung, 73, 212–285, 1955.
Zhao, H. F., Zhang, L. M., and Chang, D. S.: Behavior of coarse widely graded soils under low confining pressures, Journal of Geotechnical and Geoenvironmental Engineering, ASCE, 139, 35–48, 2013.

GMDD
7, 7267–7316, 2014
EDDA

H. X. Chen and
L. M. Zhang

Table 1. Soil properties in Test 3, Test 4 and field application.

Test No.	c' (kPa)	d_{50} (mm)	ρ_w ($kg\,m^{-3}$)	ρ_s ($kg\,m^{-3}$)	ϕ (°)	ϕ_{bed} (°)	s_b	C_{v*}	K_e ($m^3\,(Ns)^{-1}$)
Test 3	0	1.66	1000	2650	37	37	1	0.655	5×10^{-5}
Test 4	0	3.08	1000	2650	35	35	1	0.650	2.5×10^{-5}
Field application	0	35	1000	2750	37	37	1	0.65	6.6×10^{-5}

GMDD
7, 7267–7316, 2014

H. X. Chen and
L. M. Zhang

Table 2. Hydrological parameters for simulating the erosion and deposition processes in Test 3, Test 4 and field application.

Test No.	C_s	α_1 (Pa s)	β_1	K	n	δ_d
Test 3	0.4	0.02	2.97	500	0.1	NA
Test 4	0.4	0.02	2.97	500	0.05 and 0.1	0.01
Field application	0.5	0.02	2.97	2500	0.16	0.02

GMDD
7, 7267–7316, 2014

H. X. Chen and
L. M. Zhang

Table 3. Hydrological parameters for rainfall–runoff and debris flow runout simulations in field application.

Simulation type	Manning coefficient	Initial saturation	Final saturation	Soil porosity	Initial abstraction (mm)	Saturated hydraulic conductivity ($mm\,h^{-1}$)	Soil suction head (mm)
Rainfall runoff	0.3	0.33	1.0	0.35	6	3.6	51
Debris flow	0.16	1.0	1.0	0.35	0	NA	NA

GMDD
7, 7267–7316, 2014

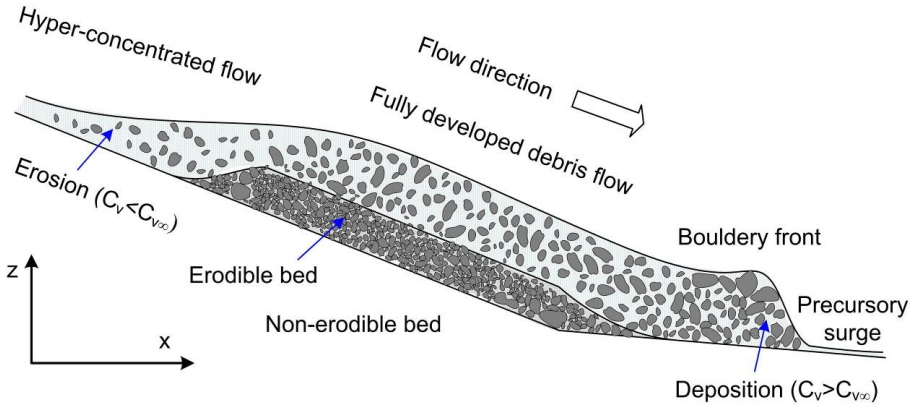

Figure 1. Erosion, deposition and property changes in debris flow.

GMDD
7, 7267–7316, 2014
EDDA

H. X. Chen and
L. M. Zhang

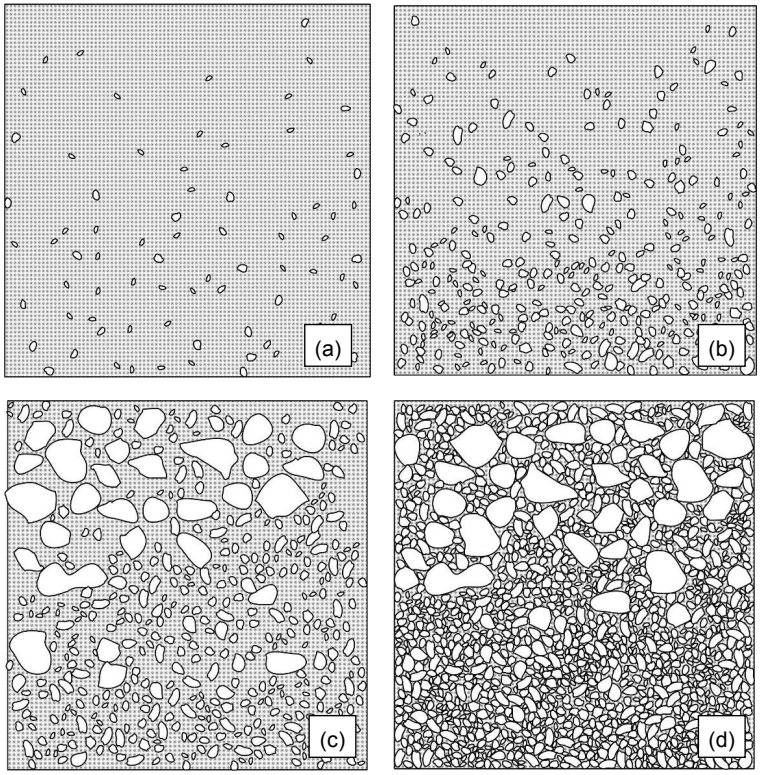

Figure 2. Changes of volumetric sediment concentrations of debris flow: **(a)** clear water flow; **(b)** hyper-concentrated flow; **(c)** fully developed debris flow; **(d)** deposit.

GMDD
7, 7267–7316, 2014

H. X. Chen and
L. M. Zhang

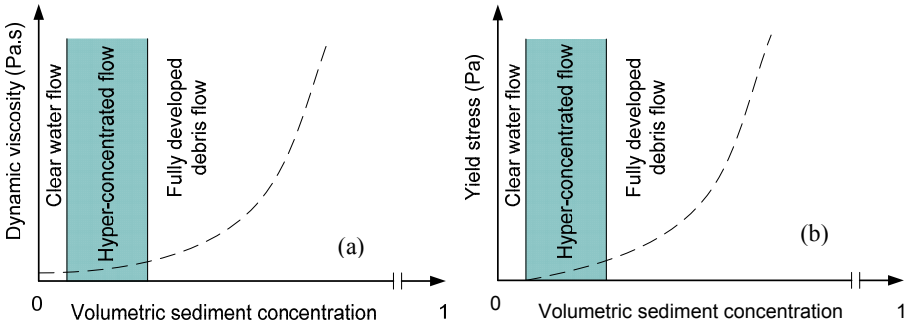

Figure 3. Changes in dynamic viscosity and yield stress with volumetric sediment concentration: **(a)** dynamic viscosity; **(b)** yield stress.

GMDD
7, 7267–7316, 2014
EDDA

H. X. Chen and
L. M. Zhang

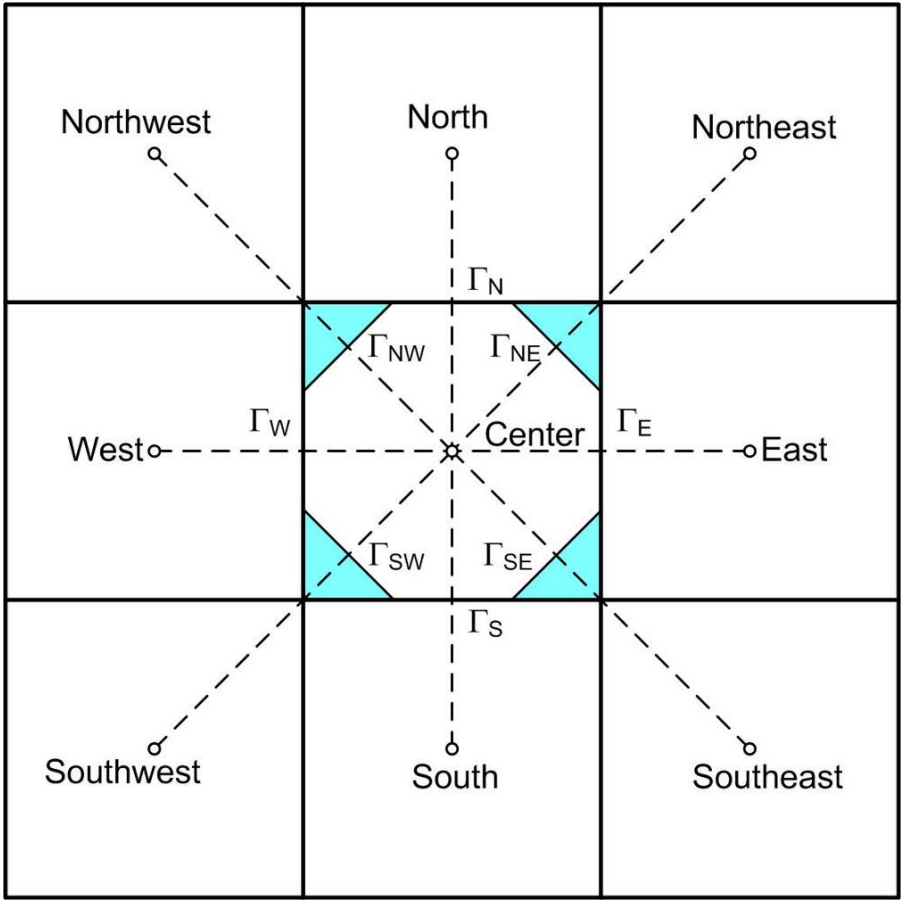

Figure 4. Eight flow directions and flow boundaries of each cell.

GMDD
7, 7267–7316, 2014
EDDA

H. X. Chen and
L. M. Zhang

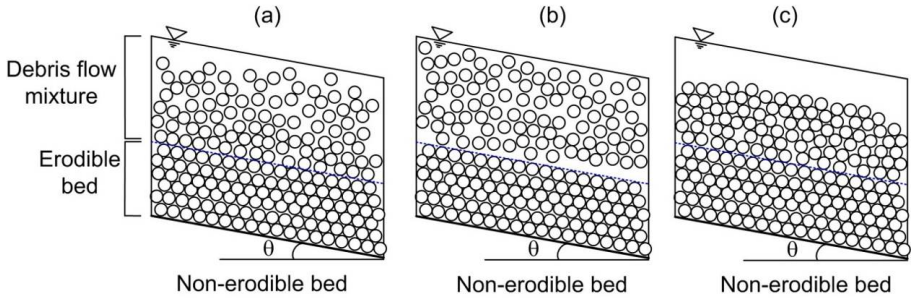

Figure 5. Three typical suspension scenarios: **(a)** partial suspension, $0 < C_s < 1$; **(b)** full suspension, $C_s = 1$; **(c)** no suspension, $C_s = 0$.

GMDD
7, 7267–7316, 2014
EDDA

H. X. Chen and
L. M. Zhang

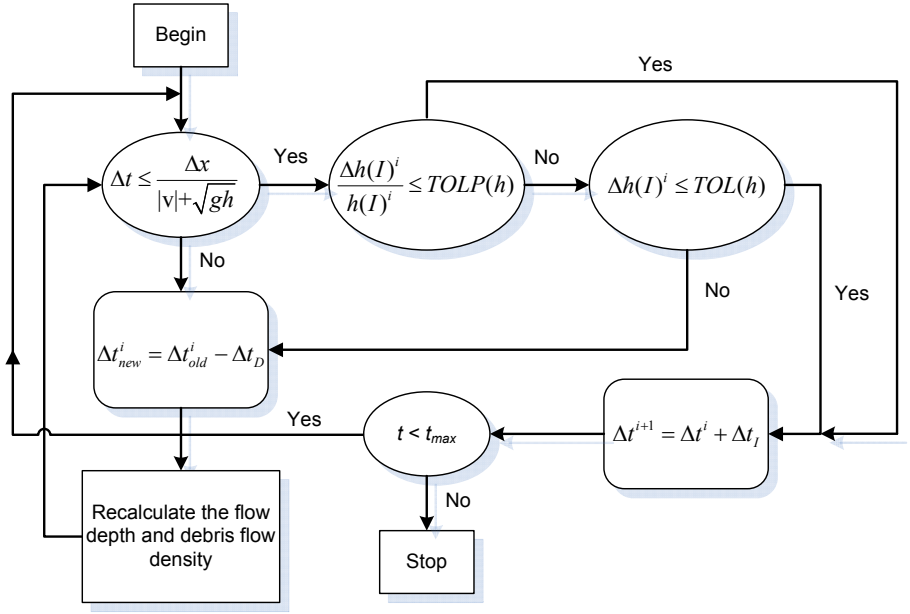

Figure 6. Algorithm for variable time step. *I*: cell *I*; $\Delta h(I)^i$: change of flow depth of cell *I* during time step *i*; $h(I)^i$: flow depth of cell *I* during time step *i*; TOLP(*h*): tolerable value of percent change of flow depth during a time step; TOL(*h*): tolerable value of change of flow depth during a time step; Δt_I: increment of time step; Δt_D: decrement of time step.

GMDD
7, 7267–7316, 2014
EDDA

H. X. Chen and
L. M. Zhang

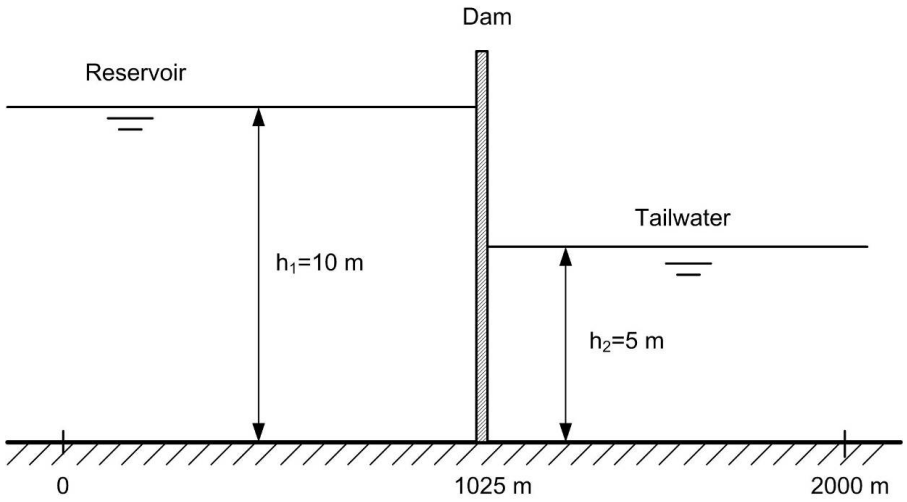

Figure 7. Definition of the one-dimensional dam-break water flow problem in Test 1.

GMDD
7, 7267–7316, 2014
EDDA

H. X. Chen and
L. M. Zhang

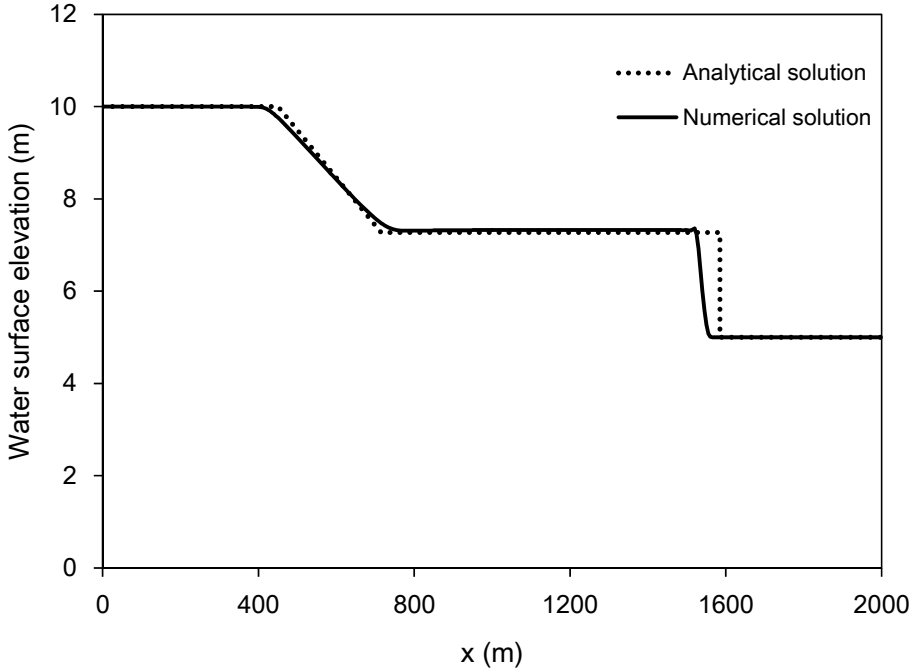

Figure 8. Comparison of water surface elevations at $t = 60$ s between the analytical solution and the numerical solution to the one-dimensional dam-break water flow problem in Test 1.

GMDD
7, 7267–7316, 2014
EDDA

H. X. Chen and
L. M. Zhang

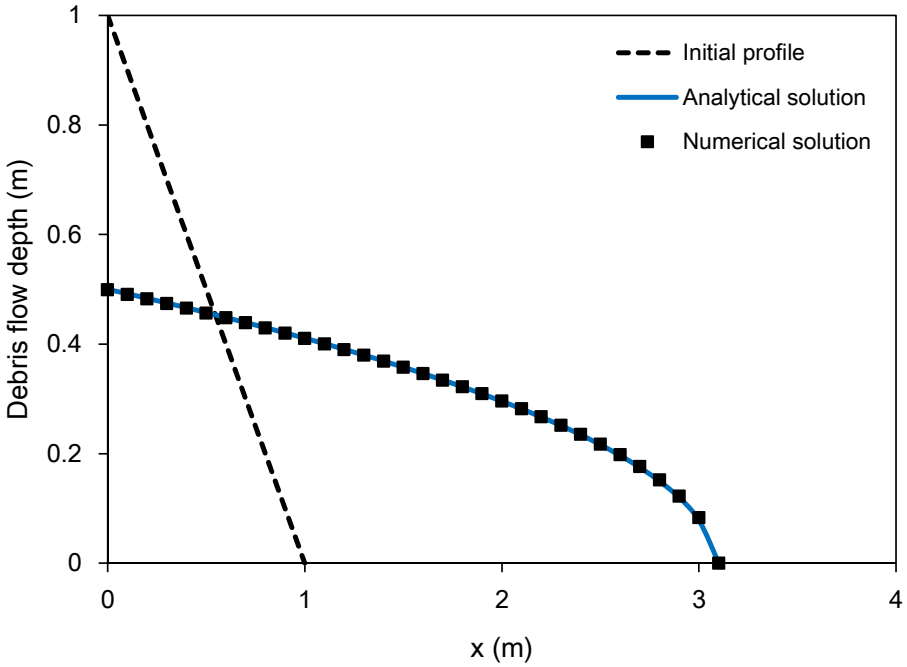

Figure 9. Comparison of the final debris flow depth profiles from the analytical solution and the numerical solution in Test 2.

GMDD
7, 7267–7316, 2014

H. X. Chen and
L. M. Zhang

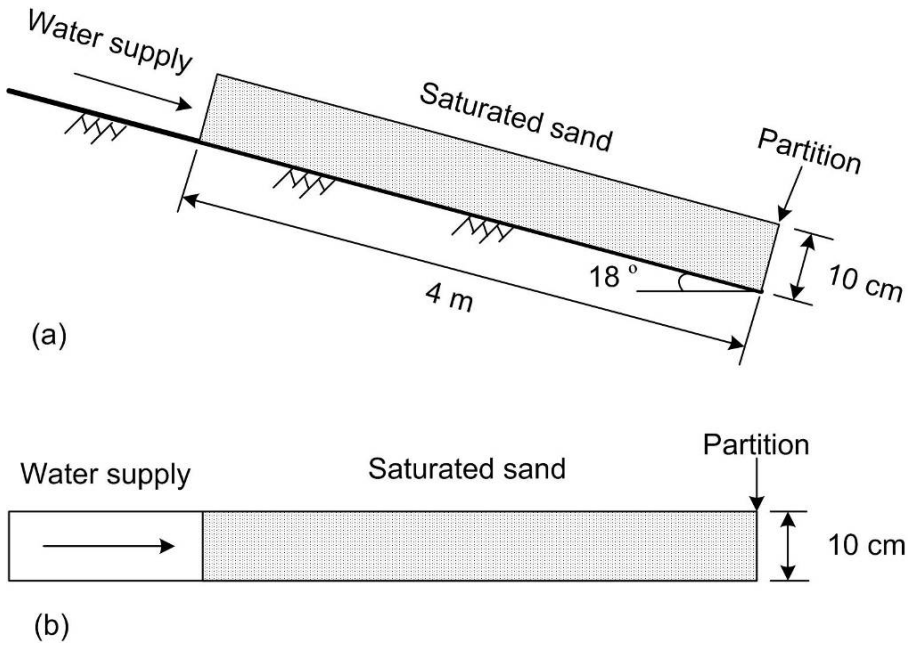

Figure 10. Experiment setup in Test 3: **(a)** side view; **(b)** bird view.

GMDD
7, 7267–7316, 2014
EDDA

H. X. Chen and
L. M. Zhang

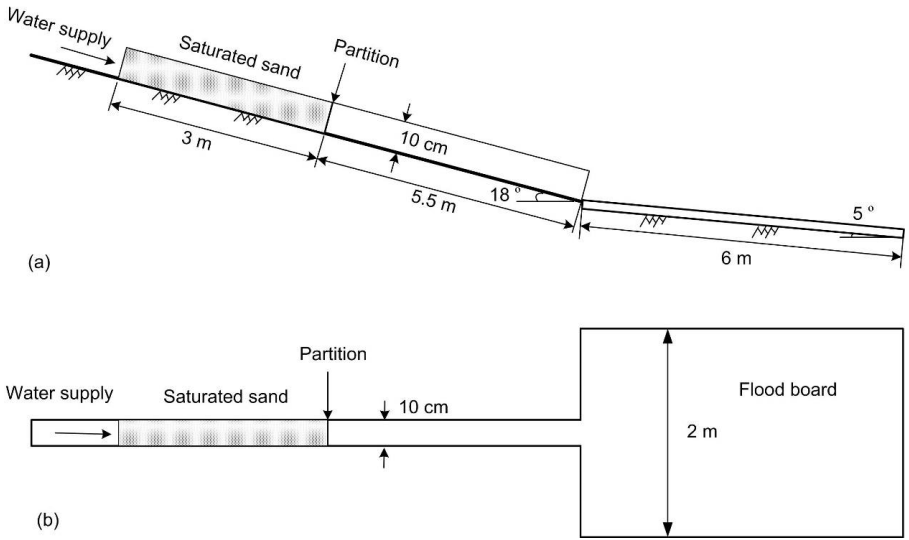

Figure 11. Experiment setup in Test 4: **(a)** side view; **(b)** bird view.

GMDD
7, 7267–7316, 2014
EDDA

H. X. Chen and
L. M. Zhang

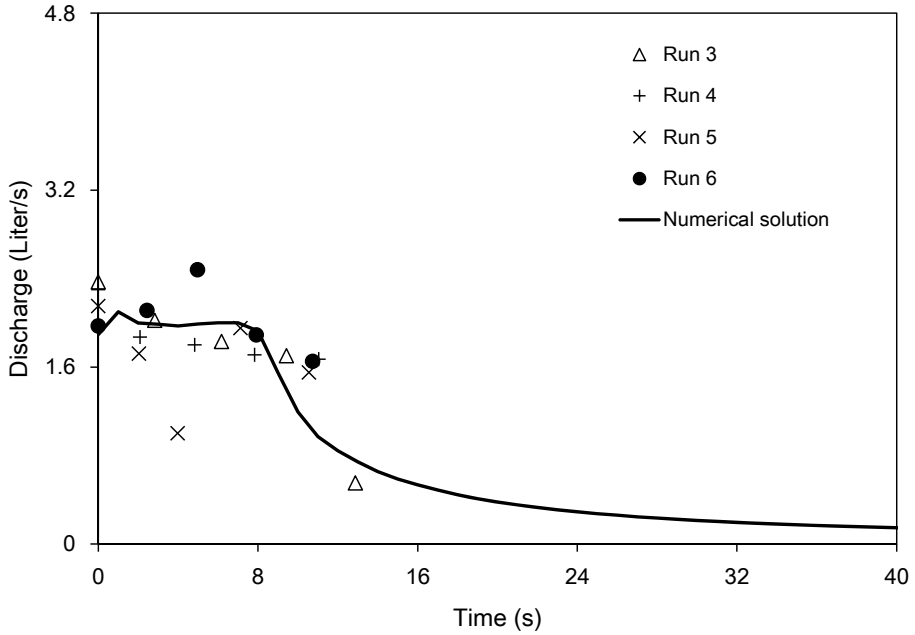

Figure 12. Comparison of discharge hydrographs at the downstream end of the flume in Test 4.

GMDD
7, 7267–7316, 2014

H. X. Chen and
L. M. Zhang

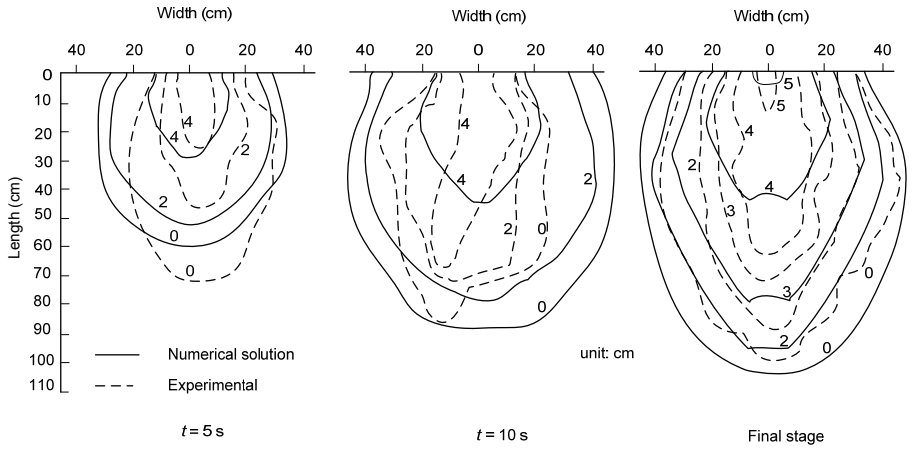

Figure 13. Comparison of the time-varying geometry and elevations of the debris fan in Test 4 from the numerical solution and the experimental tests.

GMDD
7, 7267–7316, 2014
EDDA

H. X. Chen and
L. M. Zhang

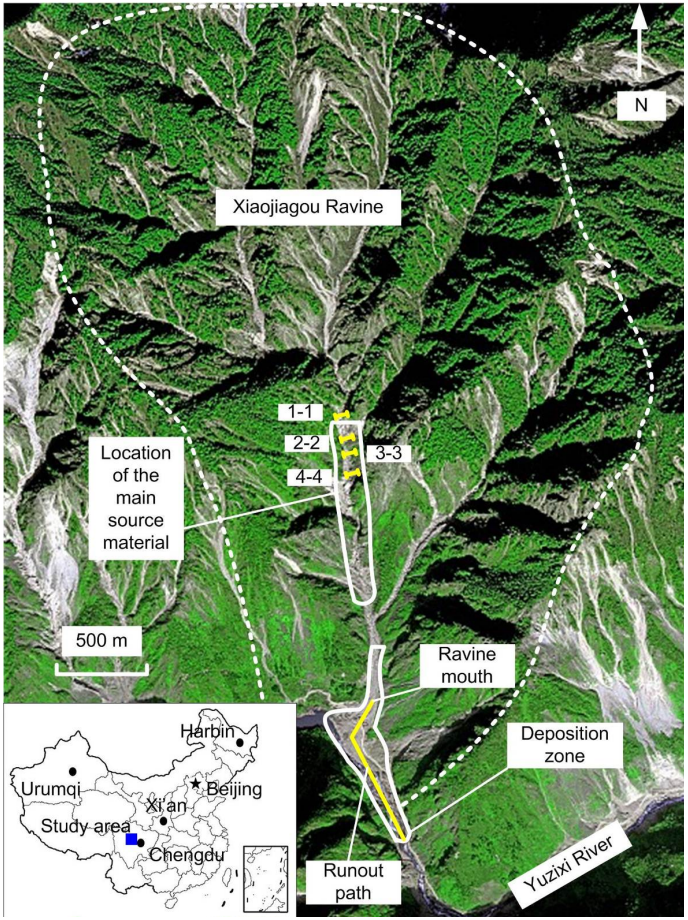

Figure 14. Location of the study area and a satellite image shortly after the Xiaojiagou debris flow.

GMDD
7, 7267–7316, 2014
EDDA

H. X. Chen and
L. M. Zhang

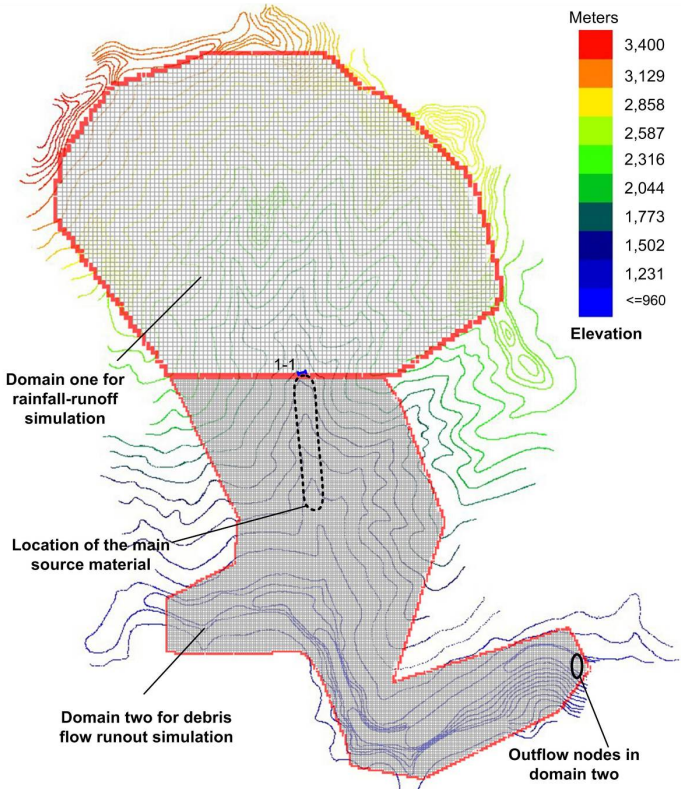

Figure 15. Grid system for rainfall runoff simulation and debris flow runout simulation.

GMDD
7, 7267–7316, 2014
EDDA

H. X. Chen and
L. M. Zhang

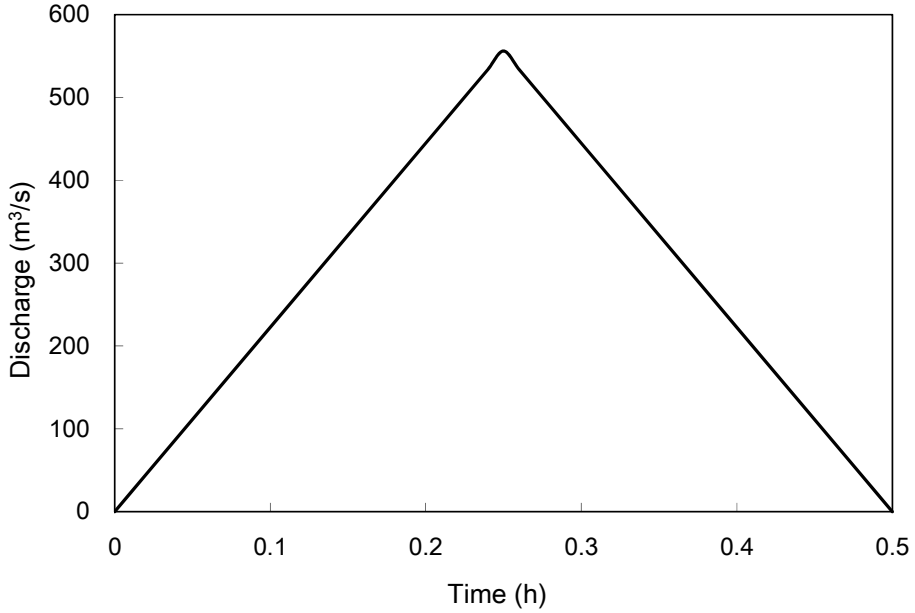

Figure 16. Surface water inflow hydrograph for debris flow runout simulation.

GMDD
7, 7267–7316, 2014
EDDA

H. X. Chen and
L. M. Zhang

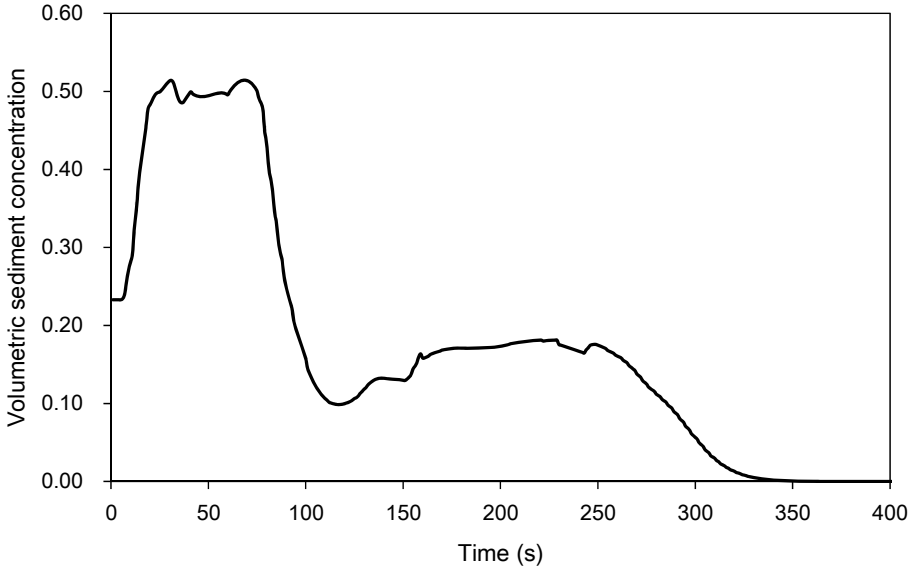

Figure 17. Change of volumetric sediment concentration at Sect. 3-3 in Fig. 14.

GMDD
7, 7267–7316, 2014
EDDA

H. X. Chen and
L. M. Zhang

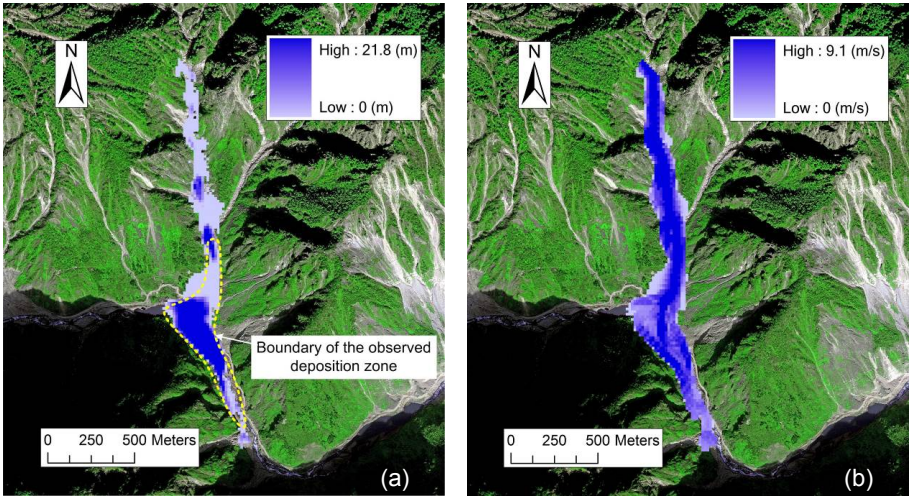

Figure 18. Simulation results of the Xiaojiagou debris flow: **(a)** final shape and depth of the deposition zone; **(b)** distribution of the maximum flow velocity.

GMDD
7, 7267–7316, 2014
EDDA

H. X. Chen and
L. M. Zhang